Coarse Grained End Bridging Monte Carlo Simulations of Poly(ethylene terephthalate) Melt

Kazunori Kamio[†] **and Krzysztof Moorthi***

Computational Science Department, Materials Science Laboratory, Mitsui Chemicals, Inc., 580-32 Nagaura, Sodegaura City, Chiba 299-0265 Japan

Doros N. Theodorou[‡]

Department of Materials Science and Engineering, School of Chemical Engineering, National Technical University of Athens, 9 Heroon Polytechniou Street, Zografou Campus, Athens GR 15780, Greece

Received April 10, 2006; Revised Manuscript Received October 9, 2006

ABSTRACT: Coarse-grained interaction potentials for poly(ethylene terephthalate) (PET) have been developed using the concept of potential of mean force and employing results of atomistic molecular dynamics simulations of ethylene terephthalate dimer. The end bridging Monte Carlo method has been adopted to handle coarse-grained PET chains. The resulting method permits for thorough, multiscale equilibration of a 100-mer PET melt, and is applicable to a wide range of industrially important polymers. The coarse-grained melt density, characteristic ratio and other conformational properties agree with experiment. Topological analyses of the melt using the CReTA and Z algorithms reveal that the melt is also well equilibrated with respect to entanglement density.

1. Introduction

Poly(ethylene terephthalate)- (PET-) based resins are used for manufacturing fibers, films, and soft drink bottles and as replacements for commodity metals such as steel and aluminum.[1−3] Although a large number of experimental studies addressing structural, dynamic, and barrier properties of PET are available, computational studies are scarce. Conformational properties of a single chain,[4−6] structure and relaxation behavior of amorphous PET,[7−9] high-temperature gas diffusivity in amorphous PET,[10,11] and oxygen diffusivity in PET and PEI glasses[9] have been the major subjects of these studies.

The physical properties of polymeric systems often depend on several length scales. Therefore, in order to extract meaningful properties from molecular simulations, the polymeric systems must be equilibrated at all length scales relevant to the problem. Hofmann et al.[12] have proposed an equilibration methodology, which is based on relaxing the polymer samples by subjecting them to long sequences of annealing−cooling and compression−decompression cycles. The melt or glass samples prepared in this way are perfectly suitable for diffusivity simulations.[9,12] However, since the standard molecular dynamics (MD) method has been used, the equilibration rate of this method is limited by the physical dynamics of the system. Assuming that the CPU time scales with the number of atoms N as $N^{1.5}$, the equilibration time of long chain features in the entangled regime by this method would approximately scale as N^5, which limits its use.

Much faster equilibration is possible by alternative methods, which are not limited by the physical dynamics of the system. Pant and Theodorou[13] developed an End Bridging (EB) as an extension of the concerted rotation (ConRot) move,[14] which enabled major changes of chain connectivity in continuum Monte Carlo (MC) simulations in a thermodynamically consistent fashion. Extensions of the method[15−19] have been effective in equilibrating highly entangled melts of linear and branched polyethylene (PE) of molecular weights approaching those of industrial resins. The method has been also applied to polypropylene,[18] polydienes,[20−22] and poly(ethylene oxide).[23]

In order to adapt connectivity altering Monte Carlo methods to a wide range of polymers with intricate chemical structures, of which PET is an example, in this paper we reduce the structural complexity of PET chains but retain their chemical identity as faithfully as possible using available polymer coarse-graining methodology.[24−28] For our purposes, we adopt a self-consistent iterative Boltzmann inversion (IBI) method.[27−28] The reduction of structural complexity of PET chains simplifies the process of generalizing standard (PE-like) connectivity-altering moves. Another important advantage is the reduction in the number of system degrees of freedom, which offsets lower acceptance rates due to the larger bulkiness and stiffness of the PET backbone. By testing the scaling properties of Kuhn lengths of subchains we find that the resulting method thoroughly equilibrates a melt composed of 100-mer PET chains at all chain length scales. The coarse-grained melt density, characteristic ratio and other conformational properties agree well with experiment. Topological analyses of the melt using the CReTA[30] and Z[31] algorithms reveal that the melt is also well equilibrated with respect to entanglement density. The distribution of reduced entanglement spacings for PET melts falls on the analogous distributions for polyethylene and polybutadiene melts, which supports Tzoumanekas and Theodorou's hypothesis[30] of a universal character for this distribution.

2. Methods

2.1. Mapping Scheme. The united-atom model of Boyd et al.[7−8] has been used as a starting point for all calculations. Figure 1a presents the mapping scheme for coarse-graining of one repeat unit of PET. Four beads are employed to represent the coarse-grained PET repeat unit: one A bead for the ethylidene group (CH_2-CH_2), two B beads for the carbonyl groups, and one C bead for the phenylene group. The A and C beads are located at the centers of mass of the ethylidene and phenylene groups, respectively, whereas B beads are placed at the centers of carbonyl carbon atoms. Since in the terephthalate moiety ($O_2C-Ph-CO_2$), energy-minimized

* Corresponding author. E-mail: Krzysztof.Moorthi@mitsui-chem.co.jp.
[†] E-mail: Kazunori.Kamio@mitsui-chem.co.jp.
[‡] E-mail: doros@chemeng.ntua.gr.

10.1021/ma060803s CCC: $37.00
Published on Web 01/06/2007

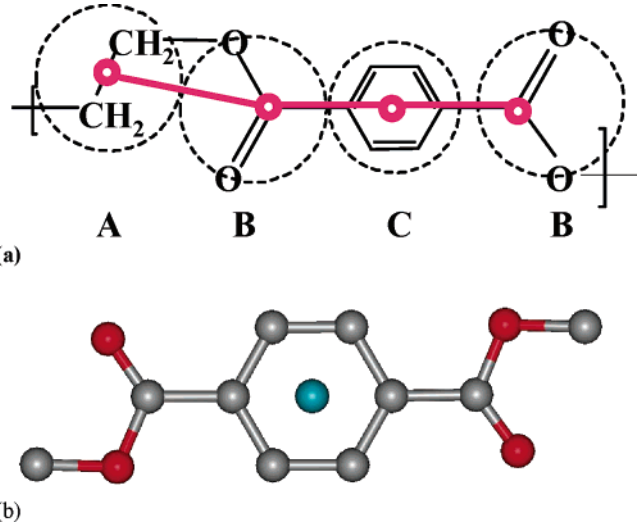

Figure 1. (a) Schematic representation of the mapping scheme for coarse-graining of one repeat unit of PET. The atomic moieties in large circles are reduced to coarse-grained beads denoted by small circles placed at the centers of mass of A and C moieties and at the center of the carbonyl carbon atom for moiety B. (b) Minimum energy structure of terephthalate moiety obtained using Boyd et al.[7−8] atomistic model. The angle between carbonyl carbons and the mass center of phenylene ring (blue bead) is 180°.

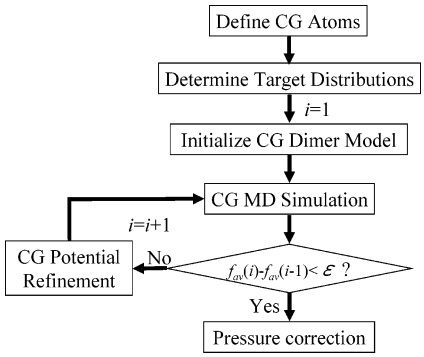

Figure 2. Flow diagram of the iterative Boltzmann inversion method.

using Boyd et al.[7−8] atomistic potentials, the carbonyl carbons and center of mass of the phenylene group are to a very good approximation collinear (Figure 1b), the BCB angle has been constrained to 180°. The C center is constrained always to lie exactly in the middle of the B−B distance (which is variable); each C bead is always connected to two BA sequences. Thus, the coarse-grained unit has only three independent bond distances (two AB and one BB) and three bond angles (two ABB and one BAB). Because of the assumed spherical symmetry of B beads, the torsional degrees of freedom ABCB and BCBA vanish, and the coarse-grained repeat unit ...B(ABCB)A... has only three torsions (one ABBA and two BABB, the C bead being excluded as BCB is collinear). Thus, this coarse-grained model has only nine degrees of freedom per repeat unit, which is significantly less than the 42 degrees of freedom per repeat unit in the united atom model of PET.[7−8] The chain sequence, $(ABCB)_nA$, is symmetrical with respect to direction reversal.

2.2. Iterative Boltzmann Inversion. Figure 2 presents the flow diagram of the iterative Boltzmann inversion (IBI) method,[28] which is used to derive the effective potentials of the coarse-grained system. The method requires knowledge of the distributions of relevant degrees of freedom, "target distributions," which are extracted from the simulations of atomistic models of polymers.[28,32−35,54] Even though oligomers of polymerization degree of only about 10 are normally used as target systems, their equilibration requires considerable computational effort, which could offset the reduction of the computational time afforded by simulating the coarse-grained polymer.

An indication that target distributions could be extracted from much shorter homologues is provided by a consideration of the rotational isomeric state model. Volkenstein[36] and Flory[37] showed that the conformational statistics of chemically detailed polymer chains are completely determined by a small number of "statistical weights." These parameters depend on torsional energies of unique bond types, their pairs or at most their triplets. This suggests that a *dimer* fluid (or a trimer one for vinyl polymers) contains sufficient information to describe all internal degrees of freedom of long polymer chains. Also, all types of nonbond interactions encountered in the polymer are already present in its dimer precursor. One could wonder why, despite the fact that the dimer and its higher homologues have exactly the same set of intra- and intermolecular interactions, the dimer *pVT* properties are known to be vastly different from those of its high-molecular weight homologues. This effect, however, is caused by changes in the concentration of chain ends, which carry an excess free volume[16,20] and should be possible to capture by a correctly coarse-grained model.

Consequently, here we extract intra- and intermolecular target distribution functions from the atomistic dimer fluid. Therefore, also the coarse-grained potentials are iteratively refined using the coarse-grained dimer fluid (Figure 2). The latter calculations are performed using the coarse-grained MD (CGMD) algorithm described in section 2.4 in the *NVT* ensemble, which further accelerates the computations. To test the validity of dimer-based CG potentials, we analyze $g(r)$'s for PET decamer fluid derived from atomistic and dimer-based CG potentials (section 3.1).

Having determined the target distributions, the effective coarse-grained potentials, $V_i(a)$ and $V_i(r)$, are refined using the differences between the distribution functions generated from the trial potentials, $P_i(a)$, $g_i(r)$, and the target distribution functions, $P^*(a)$, $g^*(r)$ (Figure 2).

$$V_{i+1}(a) = V_i(a) + k_B T \ln(P_i(a)/P^*(a)) \quad (1a)$$

$$V_{i+1}(r) = V_i(r) + k_B T \ln(g_i(r)/g^*(r)) \quad (1b)$$

where index i denotes iteration number and variable a denotes a bond length, l, bond angle, θ, or dihedral angle, ϕ, while r is an intermolecular distance. These distributions are related to their respective potentials of mean force by

$$V_{str}(l) = -k_B T \ln(P(l)/l^2) \quad (2a)$$

$$V_{bend}(\theta) = -k_B T \ln(P(\theta)/\sin\theta) \quad (2b)$$

$$V_{tor}(\phi) = -k_B T \ln(P(\phi)) \quad (2c)$$

$$V_{nb}(r) = -k_B T \ln g(r) \quad (2d)$$

where V_{str}, V_{bend}, V_{tor}, and V_{nb} are stretching, bending, torsional and nonbond contributions, respectively. The terms l^2 and $\sin\theta$ appearing in the arguments of eqs 2a and 2b arise in the Jacobian of transformation from Cartesian to generalized coordinates.

The system pressure has been adjusted by adding a linear attractive potential to the trial intermolecular potential from the fourth iteration, $V_{0ij}(r)$:

$$V_{ij}(r) = V_{0ij}(r) - Ck_B T\left(1 - \frac{r}{r_c}\right) \quad (3)$$

where $V_{ij}(r)$ is the corrected trial potential between beads of type i and j, C is an adjustable parameter, r_c is an intermolecular interaction cutoff distance, k_B is the Boltzmann constant, and T is the temperature. The potentials defined in eqs 2−3 have been smoothed using cubic splines[39] and stored in tabular form.

The convergence is monitored using an objective function which is a sum, over all coarse-grained variables x (a or r) considered, of terms of the form

$$f_{av} = 0.5f_1 + 0.5f_2 \quad (4)$$

Table 1. Simulation Protocol for Equilibrating Atomistic Dimer and Decamer Fluids

stage	conditions	dimer system duration [ns]	decamer system duration [ns]
1	*NpT*, 1 atm, 650 K	1.0	1.0
2	*NpT*, 1 atm, 650-550 K	1.0	1.0
3	*NpT*, 1 atm, 550 K	1.0	1.0
4	*NpT*, 1 atm, 550-450 K	1.0	1.0
5	*NpT*, 1 atm, 450 K	2.5	13.0
6	*NVT*, 450 K	0.1	0.1
7	*NVT*, 450 K	7.0	22.0

where

$$f_1 = D \int_{x_{min}}^{x_{max}} (A(x) - A^*(x))^2 \, dx \quad (5)$$

and

$$f_2 = \int_{x_{min}}^{x_{max}} (A(x)/A^*(x) - 1)^2 \, dx \quad (6)$$

The functions f_1 and f_2 measure absolute and relative discrepancies in trial, $A(x)$, and target, $A^*(x)$, distributions, respectively. The coefficient D has been set to 10 in order to achieve similar values of the f_1 and f_2 terms. In contrast to Reith et al.,[28] no distance-dependent weights were employed for intermolecular radial distribution function (rdf, $g(r)$) adjustment, because rdf's under the study contain peaks within the wide range of distances 3−16 Å (cf. Figure 6).

2.3. Atomistic Molecular Dynamics. The atomistic models of PET dimer fluid for deriving target potentials have been prepared by placing 15 dimer molecules in a large 50^3 Å^3 simulation cell with periodic boundary conditions. The system has been subjected to a series of *NpT* molecular dynamics runs (Table 1, stages 1−5), during which it attained equilibrium density. In the final MD run (stage 7) the end-to-end autocorrelation function vanished, indicating good equilibration of conformational properties. The atomistic models of decamer fluid have been prepared in a way similar to dimer fluids, but only four decamer molecules were used. The density equilibration of decamer fluid required longer MD runs (Table 1). Although in the final run good equilibration of decamer fluid with respect to density and $g(r)$'s has been achieved, complete decorrelation of the end-to-end vectors has not been possible. The atomistic molecular dynamics has been implemented in the LAMMPS (large-scale atomistic/molecular massively parallel simulator) program.[40] The MD simulations were executed using a velocity−Verlet integrator, Nosé-Hoover thermostat, and Nosé-Hoover barostat. The coupling constants for thermostat and barostat were 0.01 and 0.001 fs, respectively.

2.4. Coarse-Grained Molecular Dynamics. Since in the present coarse-grained PET model the BCB sequences have bending angles of 180°, the efficient integration of equations of motion for such moieties becomes an important issue. This has been achieved by treating beads of type C, which represent the benzene rings, as sites of nonbonded potentials. C beads are always constrained to lie at the midpoints of the straight line segments connecting the B beads flanking them on either side. Note that the latter segments may fluctuate in length, subject to the B−B bond length potential. These choices bring about a reduction in the number of degrees of freedom of the system to $N_f = 3(N_A + N_B) - 3$, where N_A and N_B are the number of beads of types A and B, respectively. Implementation of these constraints in a Lagrangian formulation leads to the following equations of motion for B beads

$$2m_B(2m_B + m_C)\ddot{\mathbf{r}}_{B1} = (4m_B + m_C)\mathbf{F}_{B1} - m_C\mathbf{F}_{B2} + 2m_B\mathbf{F} \quad (7a)$$

$$2m_B(2m_B + m_C)\ddot{\mathbf{r}}_{B2} = (4m_B + m_C)\mathbf{F}_{B2} - m_C\mathbf{F}_{B1} + 2m_B\mathbf{F} \quad (7b)$$

where m_B and m_C are the masses of beads B and C, respectively; $\mathbf{r}_{B1}$ and $\mathbf{r}_{B2}$, and $\mathbf{F}_{B1}$ and $\mathbf{F}_{B2}$ are the positions of and forces on beads B1 and B2; and $\mathbf{F}$ is the force vector on the interaction site C.

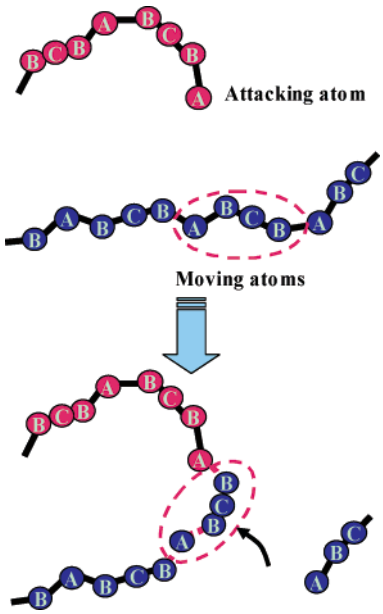

Figure 3. Schematic representation of the end bridging move for PET chain.

The above coarse-grained dynamics model has been implemented in the LAMMPS program.[40] The CGMD simulations were executed using a velocity−Verlet integrator, Nosé-Hoover thermostat, and Nosé-Hoover barostat.

2.5. End-Bridging Monte Carlo. The connectivity altering Monte Carlo program developed by Pant and Theodorou[13] and Mavrantzas et al.[15] simulates linear chains composed of only one bead type (such as polyethylene). It has been generalized here to handle linear polymers containing three bead types arranged in the $(ABCB)_nA$ sequence. This required modification of all moves and implementation of the generalized solver for the trimer reconstruction problem[19] based on the algorithm of Wu and Deem.[41] Variable bond lengths have been implemented in all moves except flip. The end-bridging move has been extended to enforce connectivity changes between monomers ABCB (Figure 3). The attacking atoms are A beads at chain ends and the victim atoms are B beads. In order to enforce the reptation of monomer units, a configurationally biased (CB) reptation move[42,53] has been implemented. The following mixture of moves has been used in simulations (percentage in parentheses denotes attempted probabilities): flips (10%), end rotations (10%), ConRot (25%), CB reptation (25%), end bridging (29.5%), and volume fluctuations (0.5%). The system pressure has been calculated from the molecular virial.[43]

2.6. Coarse-Grained Polymer Equilibration. Single chain configurations, each of degree of polymerization 100, have been generated using the continuous unperturbed chain method.[18] A system containing 10 random coils, with density 1.25 g/cm^3 has been generated. The initial configurations contained many overlaps, which have been gradually eliminated by employing the EBMC method at constant volume. Soft repulsive potentials with coarse-grained atom sizes reduced by 1.0 Å have been used at this stage. In order to prevent chain shrinkage, no attractive interactions have been employed in this phase of the calculations. The system has been relaxed for 5 million moves. Next, the original sizes of coarse-grained atoms have been restored and the system has been relaxed by performing 230 million moves of constant volume EBMC. Next, in order to accelerate the volume equilibration, the system has been subjected to 1 ns of CGMD in the *NpT* ensemble. During this pre-equilibration process the average densities have converged to 1.23 ± 0.01 g/cm^3. From this run six snapshots having density between the minimum (1.20 g/cm^3) and maximum (1.25 g/cm^3) instantaneous values have been selected as starting configurations for the final,

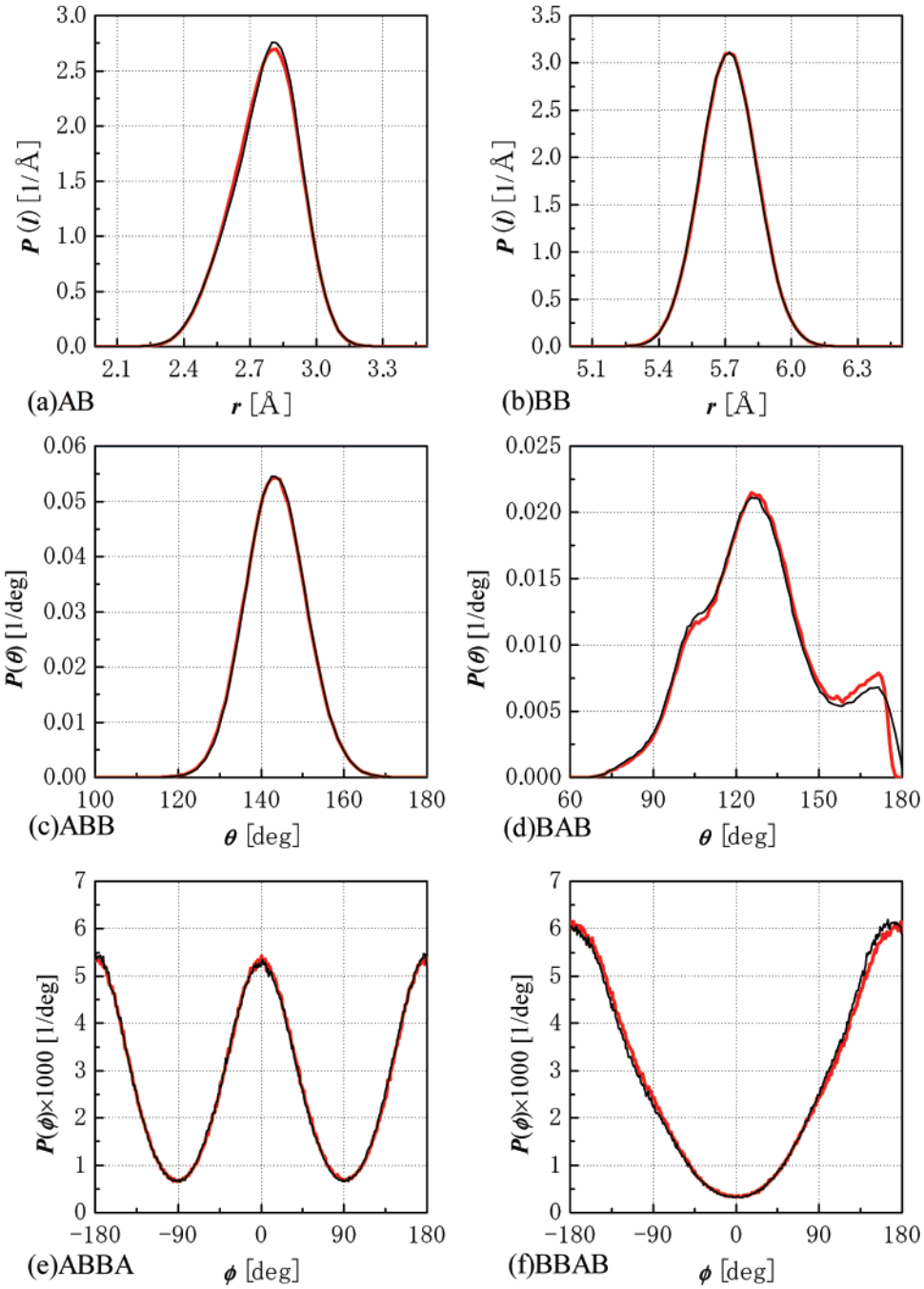

Figure 4. Distribution functions of intramolecular degrees of freedom in dimer fluid for (a) AB and (b) BB bonds, (c) ABB and (d) BAB angles, and (e) ABBA and (f) BBAB torsional angles, where 0° corresponds to the trans conformation. The thin black line represents the target distribution, and the thick red line represents the final trial distribution.

long (about 1000 million moves) EBMC runs. Since the End Bridging move employed here requires some melt polydispersity, the EBMC simulations have been performed in the semigrand $N n\mu^* pT$ ensemble.[13,18] By setting relative chemical potentials, μ^*, to zero for chains of polymerization degrees, m, $50 \le m \le 150$, and $-\infty$ outside this range, melt of a uniform molecular weight distribution centered at $\langle M \rangle = 19230$ g/mol, and varying between 9630 and 28830 g/mol has been obtained with polydispersity index $M_w/M_n = 1.08$. All results reported pertain to MC runs with MD pre-equilibration, if not explicitly specified otherwise.

2.7. Statistical Analysis of Topological Constraints. The statistical analysis of topological constraints in the PET melt has been performed using programs CReTA[30] and Z[31]. The CReTA program constructs primitive paths[44] by fixing the ends of chains in space and minimizing their contour lengths under the constraint of uncrossability. A MC algorithm employing contour straightening moves has been devised for this purpose.[30] In the course of the procedure, the chain diameter is reduced progressively down to a preset value, usually 0.5 Å. The program fully handles periodic boundary conditions, also with respect to entanglements, which is important in the case of small systems containing very long chains. The program calculates the lengths of all primitive paths, the spacings between entanglements (measured as numbers of atoms and as lengths), as well as related quantities.

The Z program constructs the primitive paths in a similar manner, but uses a deterministic contour reduction algorithm.[31] The algorithm is geometric and treats the chains as infinitely thin lines. The program calculates the length of all primitive paths in the systems and the number of entanglements per chain, Z, as well as the distances between them. The resulting primitive paths are infinitely thin. The program does not take into account entanglements between the chain in the main cell and its periodic images.

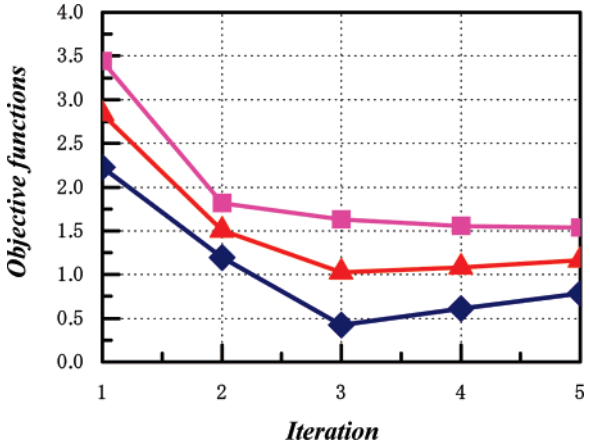

Figure 5. Changes in the objective function f_{av} (eq 4, triangles) and its components, f_1 (eq 5, diamonds) and f_2 (eq 6, squares), with respect to the number of iterations in the iterative Boltzmann inversion method for dimer fluid. In the fifth iteration, only pressure has been adjusted using eq 3.

In order to reduce finite size effects, calculations on replicas of the original cell (supercells, typically of volume 27 times higher than the original cell) have been suggested.[46]

The entanglement length, N_e, has been calculated under the assumption that the primitive path is a Gaussian coil with step length[44] $L_{pp}/(N-1)$

$$N_e = \frac{\langle R^2 \rangle}{\langle L_{pp} \rangle^2}(N-1) \tag{8}$$

where L_{pp} is the primitive path length calculated by both programs, and $\langle R^2 \rangle$ is the mean squared end-to-end distance.

The interentanglement strand length, measured in number of beads, N_{ES}, is given by[45]

$$N_{ES} = \frac{N(N-1)}{Z(N-1)+N} \tag{9}$$

where N is the number of beads in a chain and Z is the number of directly detected entanglements per chain.

3. Results and Discussion

3.1. The Coarse-Grained Potentials. The intramolecular distribution functions in the dimer fluid obtained from atomistic and CGMD simulations are given in Figure 4. Excellent convergence for all intramolecular distribution functions is observed. A small discrepancy observed for the BAB angle (Figure 4d) within the $170 < \theta < 180^o$ range is due to the fact that a slight nonzero contribution at $\theta = 180^o$ in the target distribution is neglected by forcing the trial distribution to vanish at $\theta = 180^o$. This is done in order to avoid the degeneracy of the torsional angle BBAB.

The convergence of the intermolecular radial distribution functions $g(r)$ of the coarse-grained dimer fluid model to their targets is slower than that of the intramolecular distributions. Figure 5 presents the changes of the overall objective function f_{av} and its components, f_1 and f_2, (eqs 4−6), which take into account all six intermolecular $g(r)$'s considered (AA, AB, AC, BB, BC, CC) with respect to the iteration number. Components f_1 and f_2 decreased monotonically during the first three iterations. During the fourth iteration the component f_1 increased from 0.4 to 0.6, whereas f_2 decreased slightly from 1.63 to 1.56, resulting in a very small (0.06) increase of the average objective function, smaller than the assumed convergence tolerance $\epsilon = 0.1$. This suggests that the convergence of coarse-grained intermolecular potentials to their targets could be achieved within three to four iterations. During the fifth iteration, the single value of $C = 0.209$ (eq 3) permits reducing the dimer fluid pressure to 2 atm, from the initial value of ca. 4500 atm, with only a marginal increase in the value of the average objective function f_{av} from 1.08 (iteration 4) to 1.16 (iteration 5; Figure 5). This result indicates that structural features do not change appreciably during pressure adjustment. Therefore, no further refinement of the intermolecular potentials has been considered necessary.

Figure 6 compares the target intermolecular $g(r)$'s with those calculated using coarse-grained potentials. All $g(r)$'s exhibit several extrema within the distance of 3−16 Å, which are well represented by the coarse-grained potentials fitted using the relative objective function criterion. Some discrepancies observed between the target and coarse-grained distributions could be due to the simplifications introduced (representation of a planar benzene ring and carbonyl groups by spherical coarse-grained beads).

In order to test the validity of dimer-based CG potentials, these potentials have been used in a CGMD simulation of a decamer fluid. Figures 7 and 8 compare the CG dimer-based intermolecular $g(r)$'s with $g(r)$'s derived from atomistic MD. The average root-mean-square deviations between both sets of $g(r)$'s are 0.036, 0.026, 0.032, 0.029, 0.024, and 0.045 for AA, AB, AC, BC, BB, and CC pairs, respectively, which indicates that dimer-based CG potentials afford a very good representation of structural features of the decamer fluid. Also, the density of the decamer fluid obtained using dimer-based CG potentials (1.20 g/cm^3) is in excellent agreement with the density of atomistic model of decamer (1.20 g/cm^3). Although the dimer-based CG potentials are relatively short-range (they vanish at 15 Å, cf. Figure 6), they very well represent the reduced intensity of decamer $g(r)$'s at long distances (Figures 7 and 8). This indicates that the latter effect is due to the correlation hole effect in the decamer fluid. The use of the dimer fluid as a reference avoids the possibility of including in IBI contributions to CG potentials due to the correlation hole effect. The observed very good representation of liquid structure of the decamer fluid by dimer-based CG potentials suggests that dimer-based CG potentials are transferable to polymer. This is presumably due to the fact that the PET monomer unit is still represented by several coarse-grained beads. The derivation of dimer-based CG potentials is computationally less demanding than the derivation of decamer-based ones, because of the shorter interaction range and faster equilibration of the dimer fluid.

3.2. Equilibration Efficiency and Properties at Equilibrium. Chain Conformation. The acceptance rates of the ConRot, CB reptation, and EB moves, 1.4, 0.008, and 0.0014%, respectively, are smaller than those observed in simulations of PE melts,[15] 15, 6.9, and 0.09%, respectively, or 1,2-polybutadiene,[22] 8.7−5.8, 7.7−3.0, and 0.018−0.011%, respectively. The much higher density of PET melt (1.25 g/cm^3 at 450 K) compared to PE (0.75 g/cm^3 at 450 K), and the stiffness of PET chains are likely reasons. Moreover, in the present simulation the CB reptation and EB moves enforce connectivity changes between coarse-grained PET repeat units of four beads, whereas in the PE model the reptation move alters connectivity between single beads and the EB move between their triplets. The variability of bond lengths causes a decrease in ConRot acceptance rate.

It is difficult to decorrelate large length scale features of polymer chains, such as end-to-end vectors, using methods that preserve the physical dynamics of the system. Figure 9 presents

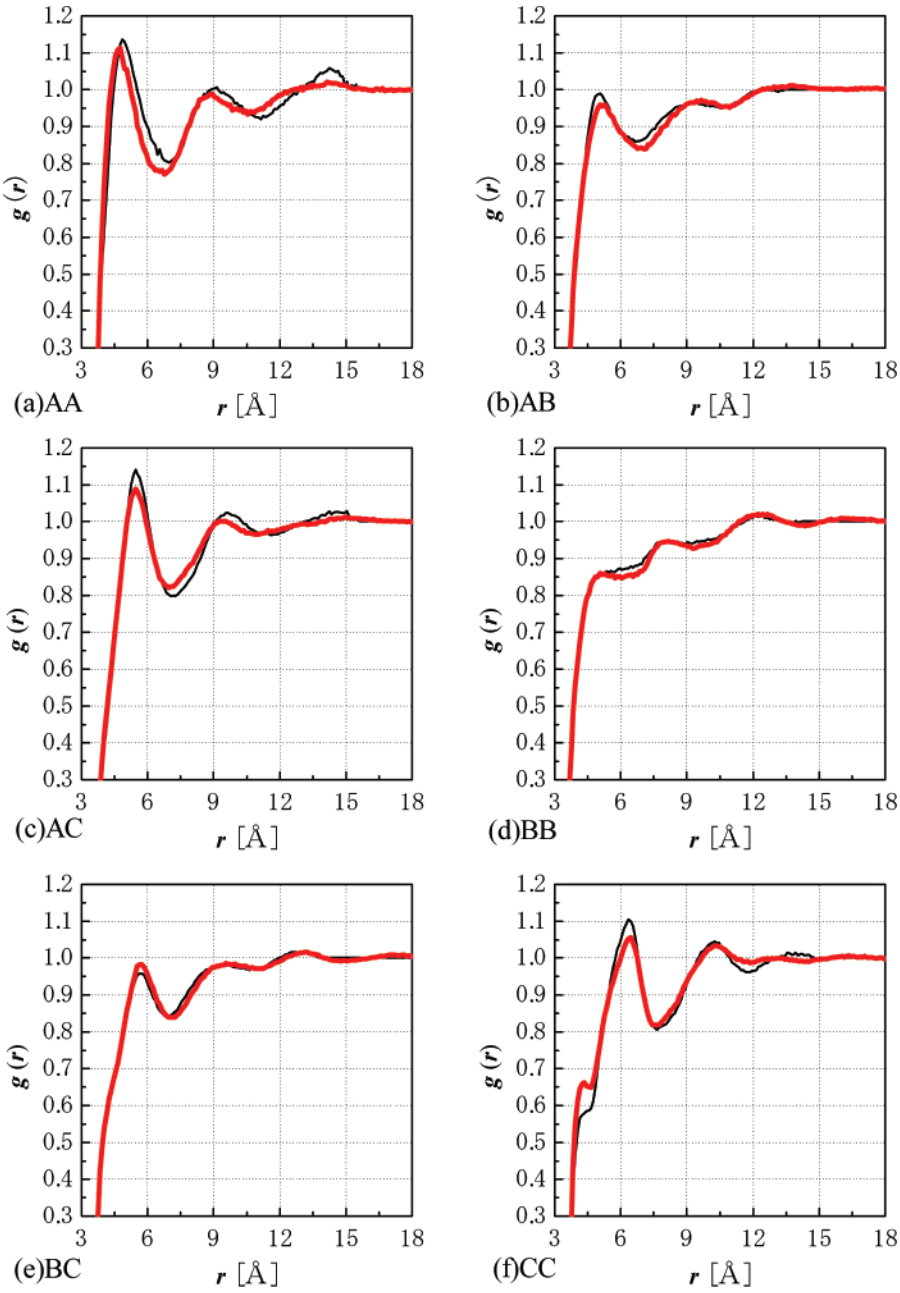

Figure 6. Intermolecular target coarse-grained radial distribution functions (thin black lines) and final adjusted radial distribution functions (thick red lines) for (a) AA, (b) AB, (c) AC, (d) BB, (e) BC, and (f) CC interactions in dimer fluid.

the decay of the orientational autocorrelation function $\langle \mathbf{u}(t)\cdot \mathbf{u}(0)\rangle$ of a unit vector directed along the chain end-to-end vector as a function of the number of Monte Carlo attempted moves for the present method. The melt of 100-mers forgets its initial end-to-end configuration in about 30 million moves. The simulation results[15] indicate that the chain end-to-end vector decorrelation in the melts of C_{200} and C_{400} PE chains is achieved in 10 and 22 million moves, respectively. These results indicate that the EB move permits to achieve a high decorrelation rate of the chain end-to-end vectors in CG PET melts, similarly as in PE melts.

Since small departures from equilibrium of the larger length scale features of chain conformations bring about an increase in free energy of the order of only few k_BT per chain, the equilibration times of these features can be very long. Auhl et al.[29] characterize the equilibration of chain features within Kuhn and end-to-end length scales by the following Kuhn length-like quantity, $l_K(N)$,

$$l_K(N) = \frac{\langle R^2(N)\rangle}{\sum_{i=1}^{n} l_i} \propto \frac{\langle R^2(m)\rangle}{m} \tag{10}$$

where $R(N)$ is the end-to-end distance of a subchain containing N beads and l_i is the bond length between beads $i-1$ and i. For well-equilibrated chains $l_K(N)$ increases monotonically with the subchain length and asymptotically reaches the chain characteristic ratio, C_∞, times the mean bond length along the contour.[29,47] The quantity $\langle R^2(m)\rangle/m$, where m is the number of repeat units in the subchain, exhibits the same properties as $l_K(N)$. Figure 10 presents $\langle R^2(m)\rangle/m$ as a function of the subchain length for combined data of six independent runs, each of length 1000 million moves. The characteristic ratio of subchains

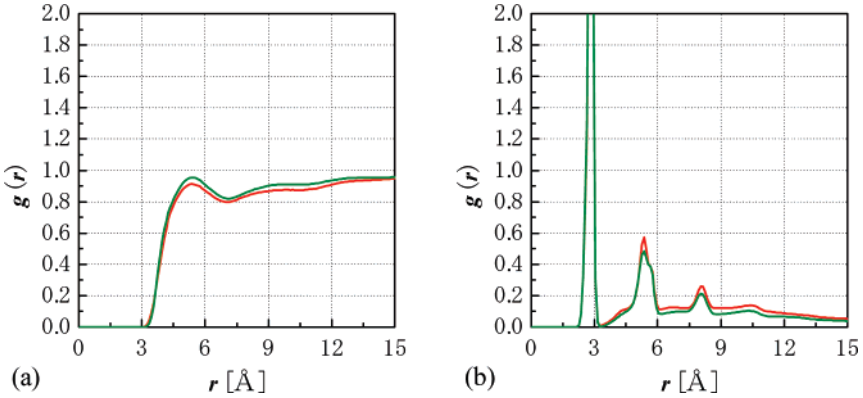

Figure 7. Comparison of the (a) total intermolecular and (b) total intramolecular radial distribution functions for decamer fluid obtained from atomistic simulation (red line) and from MD simulation with dimer-based CG potentials (green line).

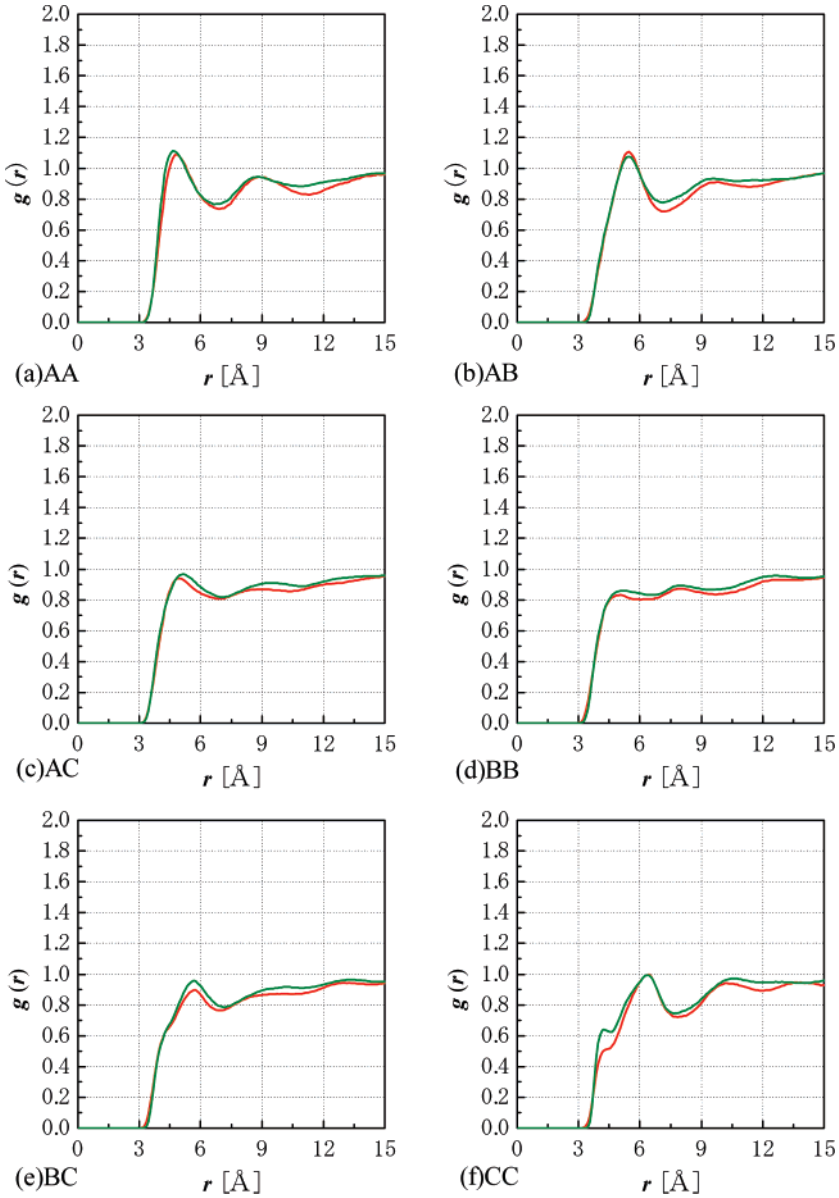

Figure 8. Comparison of the partial intermolecular radial distribution functions for decamer fluid from atomistic simulation (red line) and from MD simulation with dimer-based CG potentials (green line) for (a) AA, (b) AB, (c) AC, (d) BB, (e) BC, and (f) CC interaction sites.

increases monotonically with the subchain length within the subchain length range $1 < m < 15$. For larger subchain lengths, $15 \leq m \leq 100$, it reaches a plateau whose averaged value 140 $\pm$ 1.6 Å^2 corresponds to $\langle R^2 \rangle / M_w = 0.67 \pm 0.01$ Å^2 g^{-1} mol. The latter value is in very good agreement with the values derived on the basis of small-angle neutron scattering (SANS) measurements of PET melts; $\langle R^2 \rangle / M_w = 0.61-0.69$ Å^2 g^{-1} mol at 523 K.[48,4] These results indicate that excellent equilibration of all PET chain conformations for $m \leq 100$ has been obtained. On the other hand, for $m > 100$ the quantity $\langle R^2(m) \rangle / m$ exhibits

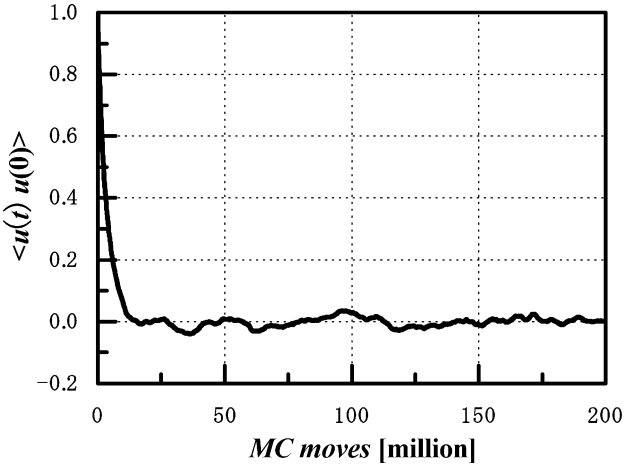

Figure 9. Orientational autocorrelation function of a unit vector parallel to the end-to-end chain vector as a function of the number of MC moves.

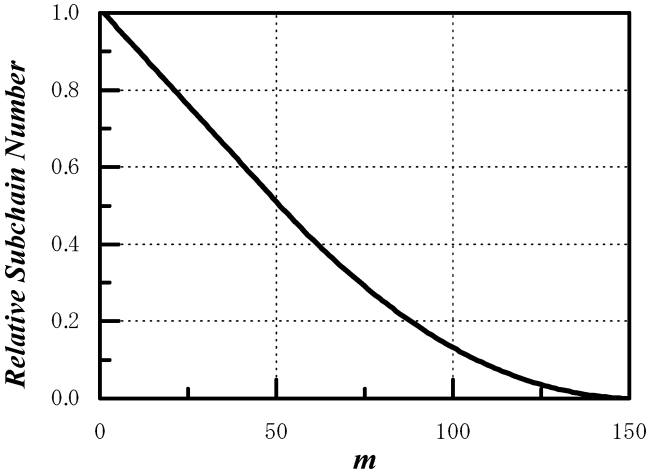

Figure 11. Number of subchains relative to that of the shortest ones ($m = 1$) as a function of their length m for combined data of six MC runs of length 1000 million moves.

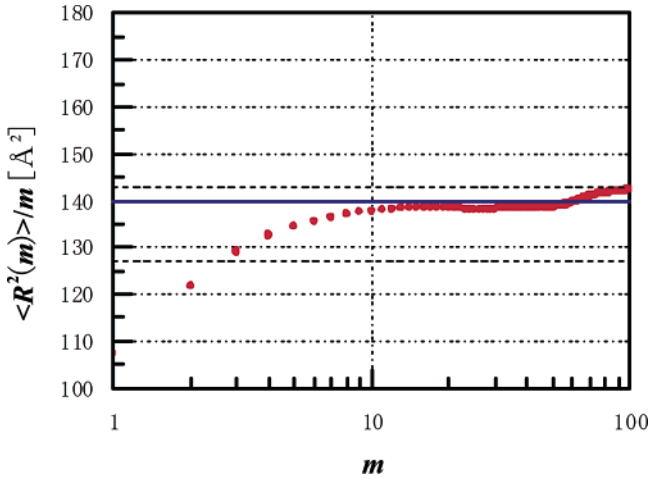

Figure 10. $\langle R^2(m)\rangle/m$ for PET subchains as a function of the number of repeat units in subchain, m. The solid line denotes the averaged plateau value corresponding to $\langle R^2\rangle/M_w = 0.67$ Å^2 g^{-1} mol. The lower and upper broken lines correspond to the experimental values of $\langle R^2\rangle/M_w$ of 0.61 and 0.69 Å^2 g^{-1} mol, respectively.[48]

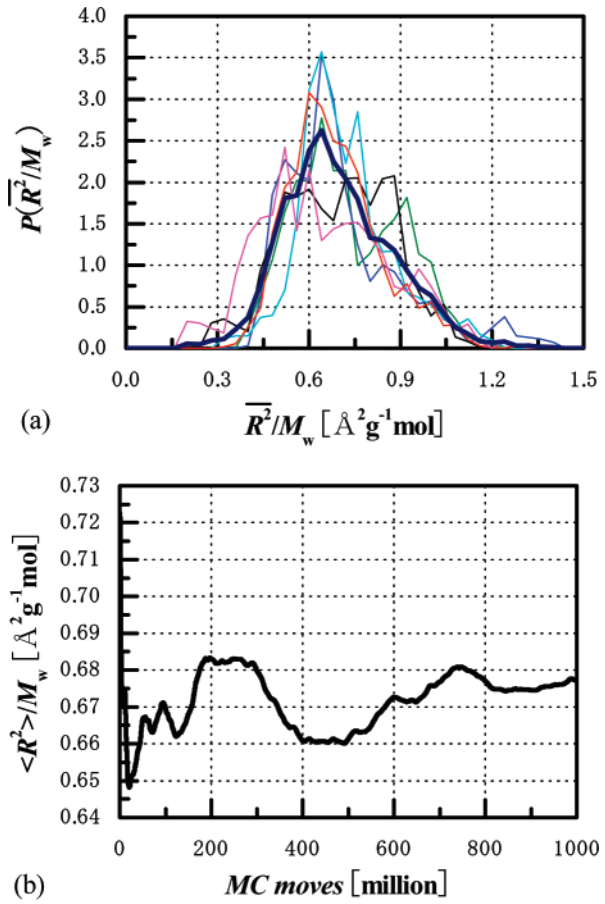

Figure 12. (a) Distributions of $\overline{R^2}/M_w$ obtained from six runs (thin solid lines) and the distribution averaged overall runs (thick line). (b) Evolution of the end-to-end chain length averaged over six independent MC runs with respect to MC number of moves.

increasing deviations from the plateau value, which are caused by a statistical noise. Because of the uniform molecular weight distribution imposed within $50 \le m \le 150$ and centered at $\langle m\rangle = 100$ (see section 2.6), for $m > 100$ the number of subchains available is very small (see Figure 11) and eventually approaches the number of longest chains in the system. Summarizing, the analysis of the end-to-end distances of subchains as a function of their length indicates that the present method permits for the excellent equilibration of the melt within all chain length scales.

Figure 12a compares the distributions of instantaneous squared end-to-end distances averaged over all chains in each snapshot, $\overline{R^2}/M_w$, obtained from six runs considered. All distributions have very similar shapes and ranges, which indicates that good equilibration has been achieved at the level of the end-to-end distances. This quantity averaged over all six runs is well conserved during the simulation (Figure 12b). The final value $\langle R^2\rangle/M_w = 0.68 \pm 0.06$ Å^2 g^{-1} mol is in excellent agreement with the value of $\langle R^2\rangle/M_w = 0.67 \pm 0.01$ Å^2 g^{-1} mol obtained from the subchain analysis and the experimental value of $\langle R^2\rangle/M_w = 0.61-0.69$ Å^2 g^{-1} mol.[48,4] These results further support our conclusions based on the analysis of subchain structural properties.

Figure 13 presents the normalized distribution function of end-to-end distances obtained by combining the simulation results from all six runs. The simulated distribution (points) is very close to the Gaussian distribution (red line). Small discrepancies from Gaussian distribution, visible for end-to-end lengths of about 100−150 Å could be due to finite chain extensibility.[37] Figure 14 presents the plot of the squared end-to-end chain lengths and radii of gyration as a function of chain degree of polymerization. Straight lines have been drawn by linear regression through the data points. Both quantities are approximately linearly dependent on the degree of polymeri-

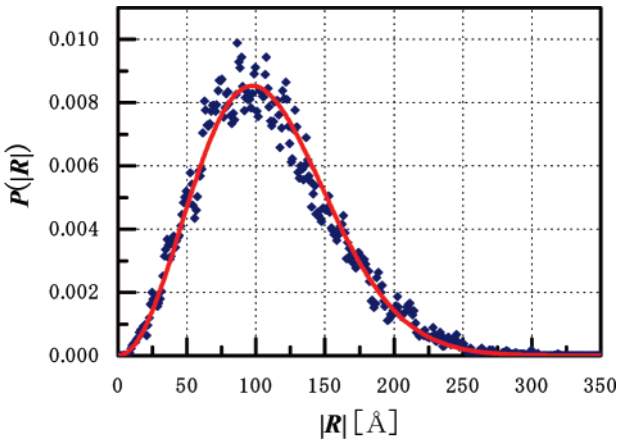

Figure 13. Comparison of the normalized probability distribution function of end-to-end distances obtained from six MC runs (points) and Gaussian distribution (red line).

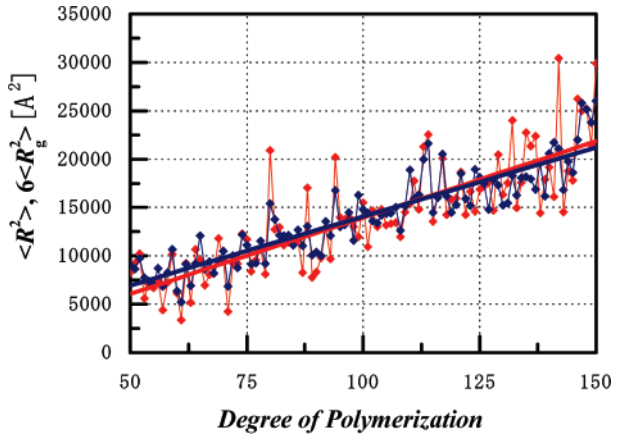

Figure 14. Dependence of the end-to-end distance (red points) and radius of gyration times six (blue points) on chain length based on the analysis of 2000 evenly spaced snapshots obtained in a single MC run of length 1000 million moves. The thin red and blue lines are guides for the eye only. The thick red and blue lines denote lines obtained from regression analysis of the end-to-end and radius of gyration data, respectively.

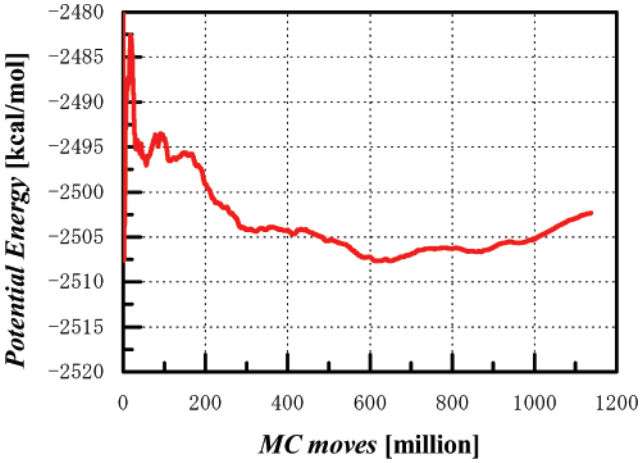

Figure 15. Evolution of the potential energy of the system averaged over six independent MC runs with respect to MC number of moves.

zation. The results in Figures 13 and 14 indicate that the chains in the simulated melt are close to unperturbed chains.

3.3. Thermodynamic Properties and Packing. Figure 15 presents the evolution of the potential energy averaged over six runs during the course of simulation. After a short initial interval of about 100 million moves was excluded, the energy

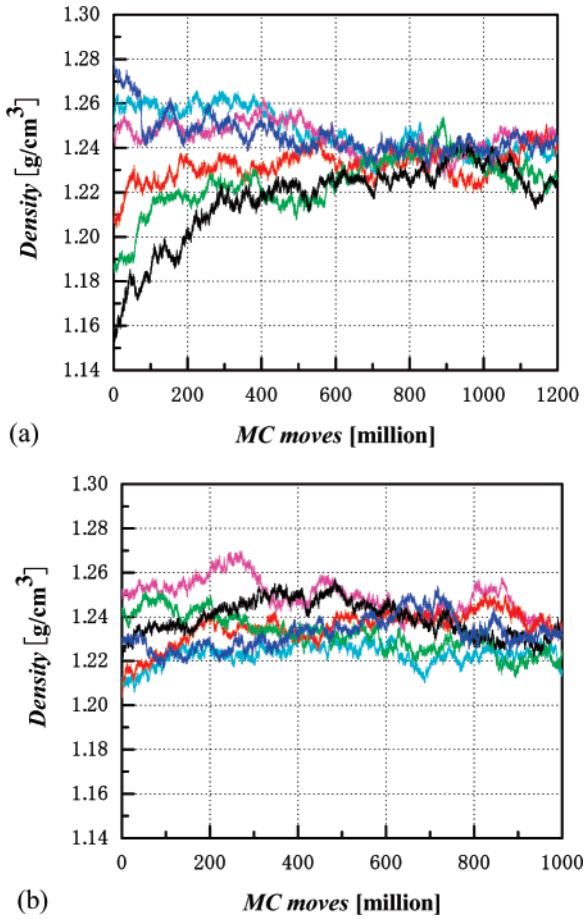

Figure 16. Evolution of CG PET melt density with MC move number for (a) six independent runs with initial configuration density varying within 1.15 and 1.28 g/cm^3 and (b) six independent runs with initial configurations as above pre-equilibrated for 1 ns with CG MD. Only the density evolution during the MC run is shown.

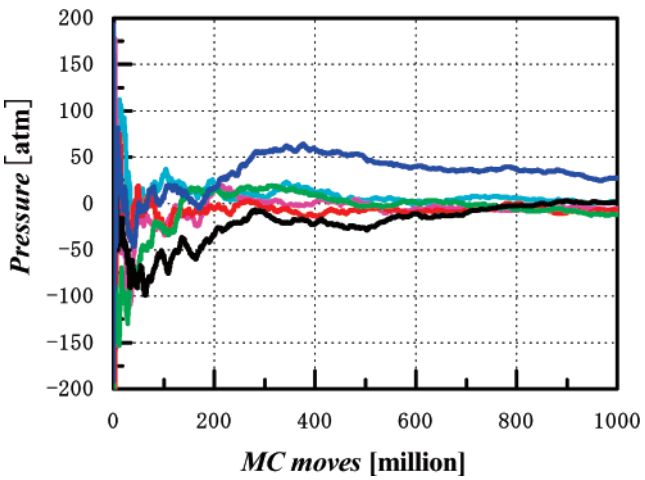

Figure 17. Evolution of CG PET melt pressure with MC move number for six MC runs.

average is conserved within ± 5 kcal/mol (about ± 0.2%). This indicates that also with respect to potential energy a very good equilibration has been achieved.

Figure 16a presents the evolution of instantaneous density obtained without pre-equilibration by CGMD. The density of initial configurations varied between 1.15 and 1.28 g/cm^3. The density of all runs converged to 1.24 ± 0.007 g/cm^3 after 600 million moves. This average density is in good agreement with a density of 1.25 g/cm^3 derived from experimental data.[49] In order to reduce the number of MC moves required to achieve

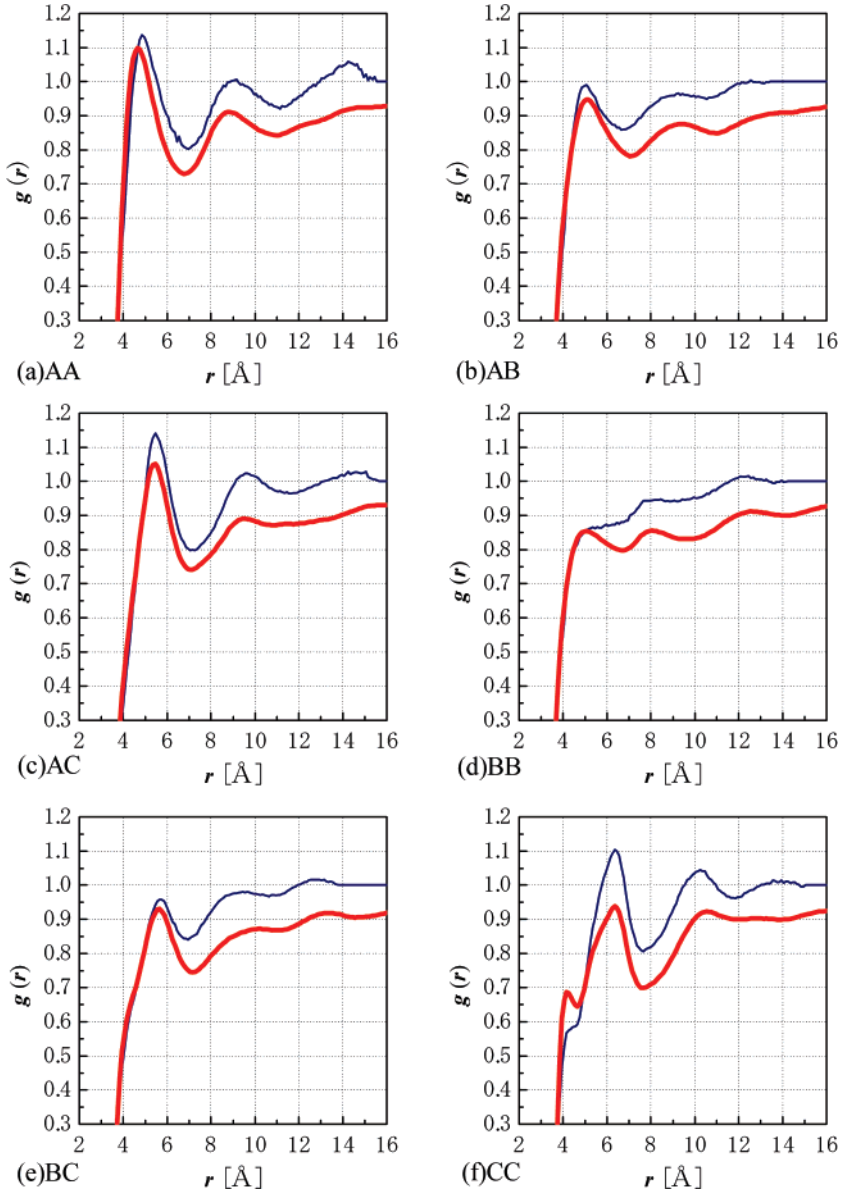

Figure 18. Comparison of the radial distribution functions of the PET melt (red lines) with those of dimer fluid (blue lines) based on the analysis of 2000 evenly spaced snapshots taken from a single MC run of length 1000 million moves.

equilibrium density, a pre-equilibration of initial configurations using MD method implemented with the same CG potentials has been considered. Figure 16b presents the evolution of the instantaneous density of the melts, pre-equilibrated for 1 ns with CGMD in *NpT* ensemble, with respect to MC number of moves. The initial configurations for the CGMD pre-equilibration runs (not shown here) were the same as those in Figure 16a. The density averaged over six $N n\mu^* pT$ EBMC runs during the first 600 million moves (Figure 16b) is 1.24 ± 0012 g/cm^3 which is in good agreement with a density of 1.25 g/cm^3 derived from experimental data and density calculated without CGMD pre-equilibration (Figure 16a). The pre-equilibration with CGMD seems to be effective in reducing MC density equilibration run by about 600 million moves (cf. Figure 16, parts a and b).

Figure 17 presents the evolution of the average pressure, as calculated through the molecular virial expression[43] during the last ($N n\mu^* PT$) stage of the MC simulation. Some inefficiency in volume equilibration is evident for one run, in which average pressure remains at the level of 27.6 atm even after 1000 million moves. Nevertheless, the pressure averaged over all simulation data, 1.07 atm, is very close to the expected value of 1 atm, which suggests that the density of 1.24 ± 0.01 g/cm^3 is indeed the equilibrium density of the coarse-grained melt. This result indicates that our modification of the IBI method, which is based on dimer target potentials, provides an excellent prediction of the high-molecular weight PET melt density.

Figure 18 compares the intermolecular radial distribution functions $g(r)$ for dimer and polymer. The positions of minima and maxima for both systems are very similar. However, the intensity of polymer $g(r)$'s is by about 10% lower compared to those of the dimer fluid. This indicates the presence of a correlation hole effect larger than in the case of decamer fluid (Figures 7 and 8). The extrapolation of the total coarse-grained intermolecular $g(r)$ (Figure 19) suggests that $g(r)$ will become 1 at the distance commensurate with the root-mean-square radius of gyration of the chains, about 50 Å in this case.

3.4. Entanglements in PET Melt. Hoy and Robbins[47] observed in their simulations that the entanglement density of melts equilibrated exclusively by molecular dynamics differed by a factor of 2−4 compared to melts equilibrated by a hybrid double bridging−MD method. Since the average molecular weight of the melt under study (19 230 g/mol) is about 5.5 times

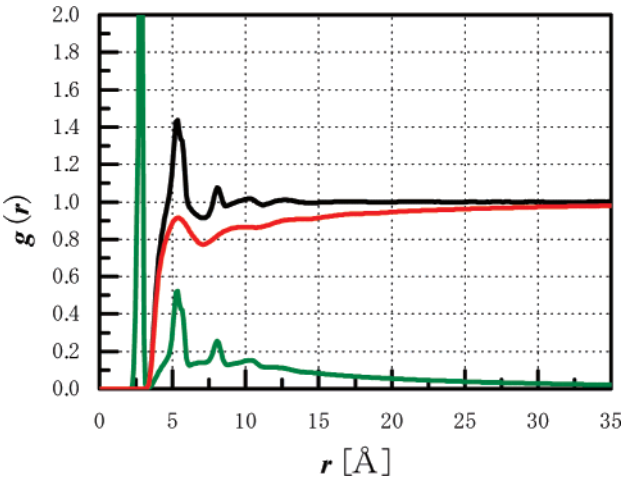

Figure 19. Total CG radial distribution functions for CG-PET. The total (black line) function is shown decomposed into intra- (green line) and intermolecular (red line) contributions.

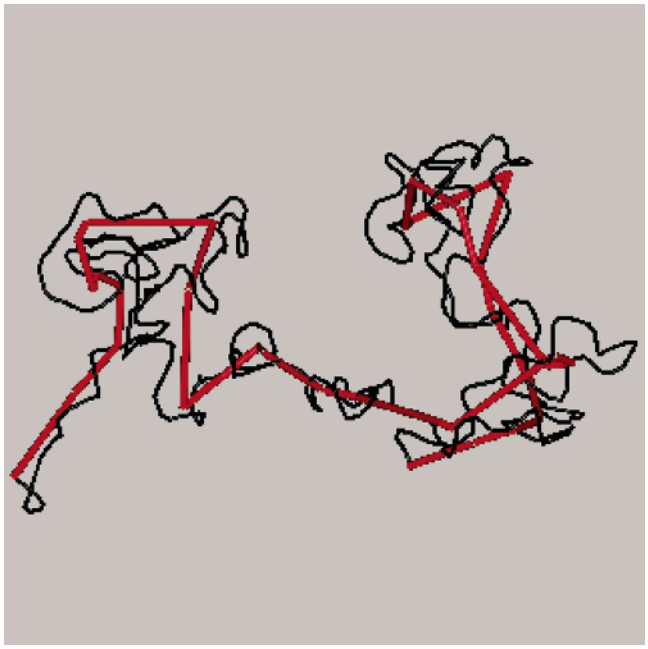

Figure 20. Representative primitive path (red line) in CG PET melt calculated using the Z algorithm[31] with the original CG PET chain (black line) superimposed. Kinks indicate the presence of constraints due to the uncrossability of neighboring chains (not shown here).

higher than the experimental critical molar mass for entanglements of PET (3500 g/mol[38]), it is worthwhile to study the evolution of entanglement density in the present melt.

Figure 20 presents an example of a calculated primitive path (thick red line) with the corresponding CG chain superimposed. As anticipated, primitive paths in the CG PET melt contain a large number of kinks, indicative of topological constraints due to chain uncrossability. Table 2, column 2, presents the statistical properties of primitive path networks calculated using the CReTA algorithm. For this analysis, data from a single run of length 800 million moves have been used. The calculated N_e value, 31.8, agrees well with those obtained applying tube theory to rheological data for the plateau modulus, $N_e = 30.2$,[50] 25,[52] and 24.4.[51] Also, the tube diameter, d, 33.5 Å, obtained computationally as the Kuhn length of the primitive path, is in excellent agreement with the literature value[50] ($d = 35$ Å). On the other hand, the N_{ES} values, which are directly related to topological melt structure, are about 2.3 times lower than the

Table 2. Statistical Properties of Primitive Path Networks in PET Melt Calculated Using CReTA[30] and Z[31] Methods

property	CReTA[a]	Z^a supercell	Z^b supercell	rheology models
$\langle L_{pp}\rangle$/Å	423.12	400.7	401.9	n.a.
d/Å	33.54	35.8	35.0	35[e] 38−43[f]
N_e	31.78	35.8	34.9	30.2[e] 24.4[f] 25.0[g]
N_{ES}	13.87	18.7[c] 15.0[d]	14.9[d]	
M_e/M_e(PE)	1.63	1.77	1.76	2.41−1.39

[a] Analysis of a single run of length about 800 million moves. [b] A total of 4800 evenly distributed snapshots taken from six runs, each about 800 million moves long. [c] Original value, uncorrected for the presence of unpaired kinks. [d] Value corrected (see text). [e] Reference 50. [f] Reference 51. [g] Reference 52.

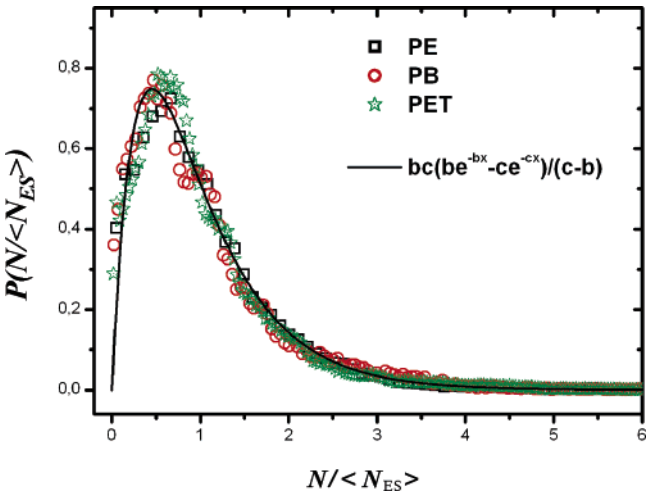

Figure 21. Normalized probability distribution of the reduced inter-entanglement strand distance, $N_{ES}/\langle N_{ES}\rangle$, measured in number of beads for PE, PB, and PET. Data for PE and PB and the theoretical line were taken from ref 30.

experimentally based N_e values. This could suggest that not all topological constraints contribute equally to the plateau modulus. Nevertheless, the PET N_{ES} values relative to the N_{ES} obtained from the analysis of long-chain (C_{1000}) PE models[30] fall within the range of rheologically based M_e(PET)/M_e(PE) ratios (Table 2). The physical significance of the N_{ES} measure is illustrated in Figure 21, which presents the distribution of reduced entanglement spacings $N_{ES}/\langle N_{ES}\rangle$ calculated by CReTA for PET melt. The distribution practically coincides with the curves for PE and 1,4-*cis*-polybutadiene, forming a single curve, which supports Tzoumanekas and Theodorou's hypothesis[30] of its universality.

Since the Z algorithm does not take into account entanglements between the chain in the main cell and its periodic images, finite cell size effects have to be assessed. An increase of the cell size by a factor of 27 causes a 10% decrease in N_e and N_{ES} values; therefore, in the subsequent discussion of the Z code results only supercell-based calculations are considered. The average primitive path length, $\langle L_{pp}\rangle$ calculated by the Z algorithm is slightly lower (402 Å) than that calculated using the CReTA program (423 Å). Thus, the CReTA-derived N_e is by about 5% lower than the Z-derived N_e. The entanglement spacing calculated by the Z algorithm directly from the number of kinks, N_{ES}, is 18.7, which is higher than the CReTA result ($N_{ES} = 13.9$). Analysis of the primitive path coordinates from the Z algorithm revealed the presence of a number of kinks, which

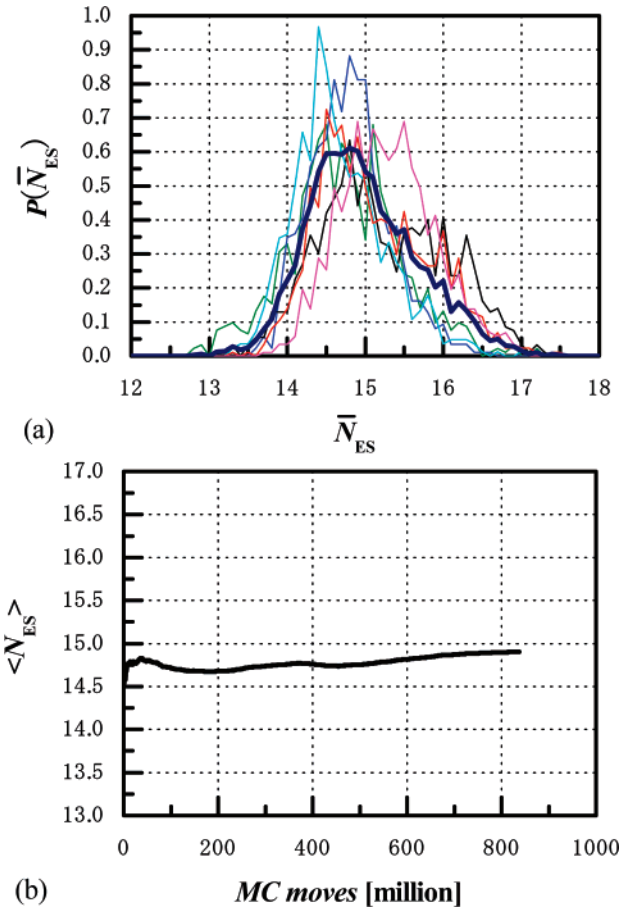

Figure 22. (a) Normalized distribution of instantaneous inter-entanglement strand length averaged over all chains in each snapshot, $\bar{N}_{ES}$, measured in number of beads, for six independent runs (thin lines) and average normalized distribution over six runs (thick line). (b) Evolution of inter-entanglement strand length, $\langle N_{ES} \rangle$, measured in number of beads, and averaged over six independent MC runs, as a function of MC number of moves.

do not have a counterpart on other chains. Such unpaired kinks occur when a primitive path forms a straight line in the vicinity of an entanglement.[31] The analysis of kink environments and resulting correction for unpaired kinks yields $N_{ES} = 15.0$, in very good agreement with the CReTA result (13.9). Thus, for the system considered, the corrections for finite size effects and for the presence of single kinks in the Z code yield primitive path lengths and entanglement spacings N_{ES} and N_e, which are in good agreement with those calculated using the CReTA algorithm.

Figure 22a presents the Z-code derived distributions of instantaneous N_{ES} averaged over all chains in each snapshot for all six runs considered after applying finite size cell and 1-kink corrections. All six distributions have very similar shapes and ranges, which indicates adequate sampling in individual runs. Figure 22b presents the cumulative average in N_{ES} for all six runs calculated using the Z algorithm, after applying the above corrections. The N_{ES} values averaged over six independent runs vary within a narrow range of $\pm 3\%$ during the course of simulation. The fourth column in Table 2 presents the statistical properties of primitive path networks averaged over all six runs and calculated using the Z algorithm. No significant differences in results from one and six runs are observed. These results indicate that very good equilibration of the melt topological structure has been achieved, as implied by the analysis of subchain Kuhn lengths (Figure 10).

4. Conclusions

A new methodology for the thorough, multiscale equilibration of chemically complex polymer melts has been proposed and verified by applying it to PET melt. In the first stage, the Iterative Boltzmann Inversion coarse-graining scheme reduces the chemical complexity of the polymer, but the structurally simpler model faithfully retains its chemical identity. This facilitates the process of generalizing standard (PE-like) connectivity-altering moves in order to equilibrate the coarse-grained PET model in the second stage. It also reduces the number of degrees of freedom in the system, which offsets lower acceptance rates of the MC scheme caused by the larger bulkiness and stiffness of the PET backbone. By deriving target distributions based on dimer models, improvement in the efficiency of the iterative Boltzmann inversion scheme has been achieved. The resulting method is applicable to a wide range of industrially important polymers.

The analysis of the subchain Kuhn length indicates that the melt is adequately equilibrated within Kuhn and chain length scale range. Also, very good conservation of potential energy and averaged end-to-end distance is observed during the simulation. Consequently, excellent equilibration at the level of topological constraints has been achieved as evidenced by highly consistent values of interentanglement spacings in all MC runs. The distribution of reduced entanglement spacing $N_{ES}/\langle N_{ES} \rangle$ calculated by the CReTA algorithm for PET melt falls on the corresponding distributions for PE and PB, which suggests its universal character as hypothesized by Tzoumanekas and Theodorou.[30]

All MC runs produce highly consistent end-to-end distances and densities, which agree well with experiment.

Acknowledgment. We thank Dr. L. Peristeras for the code of the Wu and Deem solver, Dr. Ch. Tzoumanekas for the results of CReTA calculations and the reprint of his paper prior to publication, and Prof. M. Kröger, Prof. V. Mavrantzas, and Ms. K. Foteinopoulou for the reprint of their paper prior to publication and their helpful comments on the Z code. K.K. would like to thank all members of the Computational Materials Science Laboratory of NTUA for their support during his stay there. Mitsui Chemicals, Inc. is thanked for the permission to publish this work.

References and Notes

(1) Brozenick, N. J. *Modern Plastics Encyclopedia*; McGraw Hill: New York, 1986; p 464.
(2) Jaquiss, D. B. G.; Borman, W. F. H.; Campbell, R. W. In *Encyclopedia of Chemical Technology*; Grayson, M. Ed.; Wiley: New York, 1982; Vol. 18, p 549.
(3) Margolis, J. M. *Engineering Thermoplastics: Properties and Applications*; Marcel Dekker: New York, 1986; p 42.
(4) Cail, J. I.; Stepto, R. F. T.; Taylor, D. J. R.; Jones, R. A.; Ward, I. M. *Phys. Chem. Chem. Phys.* **2000**, *2*, 4361.
(5) Tonelli, A. E. *Polymer* **2002**, *43*, 637.
(6) Tonelli, A. E. *J. Polym. Sci., Polym. Phys.* **2002**, *40*, 1254.
(7) Boyd, S. U.; Boyd, R. H. *Macromolecules* **2001**, *34*, 7219. (A value of V_2 parameter in Table 1, column 5, for O−C−C−O (IV) torsional angle has been taken as +0.8 kcal/mol).
(8) Hedenqvist, M. S.; Bharadwaj, R.; Boyd, R. H. *Macromolecules* **1998**, *31*, 1556.
(9) Karayiannis, N. Ch.; Mavrantzas, V. G.; Theodorou, D. N. *Macromolecules* **2004**, *37*, 2978.
(10) Bharadway, R. K.; Boyd, R. H. *Polymer* **1999**, *40*, 4229.
(11) Shanks, R.; Pavel, D. *Mol. Simul.* **2002**, *28*, 939.
(12) Hofmann, D.; Fritz, L.; Ulbrich, J.; Schepers, C.; Bohning, M. *Macromol. Theory Simul.* **2000**, *9*, 293.
(13) Pant, P. V. K.; Theodorou, D. N. *Macromolecules* **1995**, *28*, 7224.
(14) Dodd, L. R.; Boone, T. D.; Theodorou, D. N. *Mol. Phys.* **1993**, *78*, 961.

(15) Mavrantzas, V. G.; Boone, T. D.; Zervopoulou, E.; Theodorou, D. N. *Macromolecules* **1999**, *32*, 5072.
(16) Karayiannis, N. Ch.; Mavrantzas, V. G.; Theodorou, D. N. *Phys. Rev. Lett.* **2002**, *88*, 105503.
(17) Karayiannis, N. Ch.; Giannousaki, A. E.; Mavrantzas, V. G. *J. Chem. Phys.* **2003**, *118*, 2451.
(18) Theodorou, D. N.; In: Nielaba, P.; Mareschal, M.; Ciccotti, G. *Bridging Time Scales: Molecular Simulations for the Next Decade*; Springer, Berlin, 2002.
(19) Peristeras, L. D.; Economou, I. G.; Theodorou, D. N. *Macromolecules* **2005**, *38*, 386.
(20) Doxastakis, M.; Mavrantzas, V. G.; Theodorou, D. N. *J. Chem. Phys.* **2001**, *115*, 11339.
(21) Doxastakis, M.; Mavrantzas, V. G.; Theodorou, D. N. *J. Chem. Phys.* **2001**, *115*, 11352.
(22) Gestoso, P.; Nicol, E.; Doxastakis, M.; Theodorou, D. N.; *Macromolecules* **2003**, *36*, 6925.
(23) Wick, C. D.; Theodorou, D. N. *Macromolecules* **2004**, *37*, 7026.
(24) Tschöp, W.; Kremer, K.; Batoulis, J.; Bürger, T.; Hahn, O. *Acta Polym.* **1998**, *49*, 61.
(25) Tschöp, W.; Kremer, K.; Hahn, O.; Batoulis, J.; Bürger, T. *Acta Polym.* **1998**, *49*, 75.
(26) Fukunaga, H.; Takimoto, J.; Doi, M. *J. Chem. Phys.* **2002**, *118*, 8183.
(27) Müller-Plathe, F. *Chem. Phys. Chem.* **2002**, *3*, 754.
(28) Reith, D.; Pütz, M.; Müller-Plathe, F. *J. Comput. Chem.* **2003**, *24*, 1624.
(29) Auhl, R.; Everaers, R.; Grest, G. S.; Kremer, K.; Plimpton, S. J. *J. Chem. Phys.* **2003**, *119*, 12718.
(30) Tzoumanekas, C.; Theodorou, D. N. *Macromolecules* **2006**, *39*, 4592.
(31) Kröger, M. *Comput. Phys. Commun.* **2005**, *168*, 209.
(32) Faller, R.; Reith, D. *Macromolecules* **2003**, *36*, 5406.
(33) Milano, G.; Müller-Plathe, F. *J. Phys. Chem. B* **2005**, *109*, 18609.
(34) Queyroy, S.; Neyertz, S.; Brown, D.; Müller-Plathe, F. *Macromolecules* **2004**, *37*, 7338.
(35) Girard, S.; Müller-Plathe, F. In *Novel Methods in Soft Matter Simulations*; Karttunen, M., Vattulainen, I., Lukkarinen, A., Eds.; Springer: Berlin, 2004; p 327.
(36) Volkenstein, M. V. *Configurational Statistics of Polymeric Chains*; Interscience Publishers: New York, 1963.
(37) Flory, P. J. *Statistical Mechanics of Chain Molecules*; Hanser: Munich, Germany, 1969.
(38) Aharoni, S. M. *Makromol. Chem.* **1978**, *179*, 1867.
(39) *IMSL Fortran Subroutines*; Visual Numerics, Inc.: Houston, TX, 1997.
(40) Plimpton, S. *J. Comput. Phys.* **1995**, *1*, 117.
(41) Wu, M. G.; Deem, M. W. *J. Chem. Phys.* **1999**, *111*, 6625.
(42) Frenkel, D.; Smit, D. *Understanding Molecular Simulation*; Elsevier: Amsterdam, 2001.
(43) Theodorou, D. N.; Boone, T. D.; Dodd, L. R.; Mansfield, K. F. *Makromol. Chem., Theory Simul.* **1993**, *2*, 191.
(44) Doi, M.; Edwards, S. F. *The Theory of Polymer Dynamics*, Clarendon: Oxford, U.K., 1986.
(45) Everaers, R.; Sukumaran, S. K.; Grest, G. S.; Svaneborg, C.; Sivasubramanian, A.; Kremer, K. *Science* **2004**, *303*, 823.
(46) Foteinopoulou, K.; Karayiannis, N. Ch.; Mavrantzas, V. G.; Kröger, M. *Macromolecules* **2006**, *39*, 4207.
(47) Hoy, R. S.; Robbins, M. O. *Phys. Rev. E* **2005**, *72*, 061802.
(48) Gilmer, J. W.; Wiswe, D.; Zachmann, H.-G.; Kugler, J.; Fischer, E. W. *Polymer* **1986**, *27*, 1391.
(49) Zoller, P.; Bolli, P. *J. Macromol. Sci., Phys.* **1980**, *B18*, 555.
(50) Fetters, L. J.; Lohse, D. J.; Colby, R. H. In *Physical Properties of Polymers Handbook*; Mark, J. E., Ed.; Springer: Berlin, 2006, in press.
(51) Fetters, L. J.; Lohse, D. J.; Richter, D.; Witten, T. A.; Zirkel, A. *Macromolecules* **1994**, *27*, 4639.
(52) Lorentz, G.; Tassin, J. F. *Polymer* **1994**, *35*, 3200.
(53) Jain, T. S.; de Pablo, J. J. In: *Simulation Methods for Polymers*; Kotelyanskii, M., Theodorou, D. N., Eds.; M. Dekker: New York, 2004.
(54) Sun, Q.; Faller, R. *Macromolecules* **2006**, *39*, 812.

MA060803S